

Experimental demonstration of propagation characteristics of mid-infrared photonic crystal waveguides in silicon-on-sapphire

Yi Zou,^{1,4,*} Swapnajit Chakravarty,^{2,3,4} Parker Wray,¹ and Ray T. Chen^{1,2,5}

¹Microelectronics Research Center, Department of Electrical and Computer Engineering, University of Texas at Austin, 10100 Burnet Rd. Austin, Texas 78758 USA

²Omega Optics, Inc., Austin, Texas 78759 USA

³swapnajit.chakravarty@omegaoptics.com

⁴These authors contributed equally to the paper

⁵raychen@uts.cc.utexas.edu

*yzou@utexas.edu

Abstract: We provide the first experimental demonstration of optical transmission characteristics of a W1 photonic crystal waveguide in silicon on sapphire at mid infrared wavelength of 3.43 μm . Devices are studied as a function of lattice constant to tune the photonic stop band across the single wavelength of the source laser. The shift in the transmission profile as a function of temperature and refractive index is experimentally demonstrated and compared with simulations. In addition to zero transmission in the stop gap, propagation losses less than 20 dB/cm are observed for group indices greater than 20 below the light line while more than 300 dB/cm propagation losses are observed above the light line, characteristic of the waveguiding behavior of photonic crystal line defect modes.

2015 Optical Society of America

OCIS codes: (230.5298) Photonic crystals; (130.5296) Photonic crystal waveguides; (350.4238) Nanophotonics and photonic crystals.

References and links

1. M. Iqbal, M. A. Gleeson, B. Spaugh, F. Tybor, W. G. Gunn, M. Hochberg, T. Baehr-Jones, R. C. Bailey, and L. C. Gunn, "Label-free biosensor arrays based on silicon ring resonators and high-speed optical scanning instrumentation," *IEEE J. Sel. Top. Quantum Electron.* **16**(3), 654–661 (2010).
2. N. Skivesen, A. Têtù, M. Kristensen, J. Kjems, L. H. Frandsen, and P. I. Borel, "Photonic-crystal waveguide biosensor," *Opt. Express* **15**(6), 3169–3176 (2007).
3. W.-C. Lai, S. Chakravarty, Y. Zou, and R. T. Chen, "Silicon nano-membrane based photonic crystal microcavities for high sensitivity bio-sensing," *Opt. Lett.* **37**(7), 1208–1210 (2012).
4. W.-C. Lai, S. Chakravarty, Y. Zou, and R. T. Chen, "Multiplexed detection of xylene and trichloroethylene in water by photonic crystal absorption spectroscopy," *Opt. Lett.* **38**(19), 3799–3802 (2013).
5. W.-C. Lai, S. Chakravarty, X. Wang, C. Lin, and R. T. Chen, "Photonic crystal slot waveguide absorption spectrometer for on-chip near-infrared spectroscopy of xylene in water," *Appl. Phys. Lett.* **98**(2), 023304 (2011).
6. W.-C. Lai, S. Chakravarty, X. Wang, C. Lin, and R. T. Chen, "On-chip methane sensing by near-IR absorption signatures in a photonic crystal slot waveguide," *Opt. Lett.* **36**(6), 984–986 (2011).
7. R. Soref, "Mid-infrared photonics in silicon and germanium," *Nat. Photonics* **4**(8), 495–497 (2010).
8. R. Soref, S. J. Emelett, and A. R. Buchwald, "Silicon waveguided components for the long-wave infrared region," *J. Opt. A* **8**(10), 840–848 (2006).
9. Z. Cheng, X. Chen, C. Y. Wong, K. Xu, C. Fung, Y. Chen, and H. K. Tsang, "Mid-infrared grating couplers for silicon-on-sapphire waveguides," *IEEE Photon. J.* **4**(1), 104–113 (2012).
10. T. Baehr-Jones, A. Spott, R. Ilic, A. Spott, B. Penkov, W. Asher, and M. Hochberg, "Silicon-on-sapphire integrated waveguides for the mid-infrared," *Opt. Express* **18**(12), 12127–12135 (2010).
11. F. Li, S. D. Jackson, C. Grillet, E. Magi, D. Hudson, S. J. Madden, Y. Moghe, C. O'Brien, A. Read, S. G. Duvall, P. Atanackovic, B. J. Eggleton, and D. J. Moss, "Low propagation loss silicon-on-sapphire waveguides for the mid-infrared," *Opt. Express* **19**(16), 15212–15220 (2011).
12. A. Spott, Y. Liu, T. Baehr-Jones, R. Ilic, and M. Hochberg, "Silicon waveguides and ring resonators at 5.5 μm ," *Appl. Phys. Lett.* **97**(21), 213501 (2010).
13. C. Y. Wong, Z. Cheng, X. Chen, K. Xu, C. Fung, Y. Chen, and H. K. Tsang, "Characterization of mid-infrared silicon-on-sapphire microring resonators with thermal tuning," *IEEE Photon. J.* **4**(4), 1095–1102 (2012).

14. M. M. Milošević, M. Nedeljkovic, T. M. B. Masaud, E. Jaberansary, H. M. H. Chong, N. G. Emerson, G. T. Reed, and G. Z. Mashanovich, "Silicon waveguides and devices for the mid-infrared," *Appl. Phys. Lett.* **101**(12), 121105 (2012).
15. G. Z. Mashanovich, M. M. Milošević, M. Nedeljkovic, N. Owens, B. Xiong, E. J. Teo, and Y. Hu, "Low loss silicon waveguides for the mid-infrared," *Opt. Express* **19**(8), 7112–7119 (2011).
16. M. Nedeljkovic, A. Khokhar, Y. Hu, X. Chen, J. S. Penades, S. Stankovic, H. Chong, D. Thomson, F. Gardes, and G. Reed, "Silicon photonic devices and platforms for the mid-infrared," *Opt. Mater. Express* **3**, 1205–1214 (2013).
17. Y. Zou, H. Subbaraman, S. Chakravarty, X. Xu, A. Hosseini, W.-C. Lai, P. Wray, and R. T. Chen, "Grating-coupled silicon-on-sapphire integrated slot waveguides operating at mid-infrared wavelengths," *Opt. Lett.* **39**(10), 3070–3073 (2014).
18. J. Chiles, S. Khan, J. Ma, and S. Fathpour, "High-contrast, all-silicon waveguiding platform for ultra-broadband mid-infrared photonics," *Appl. Phys. Lett.* **103**(15), 151106 (2013).
19. Z. Cheng, X. Chen, C. Y. Wong, K. Xu, and H. Tsang, "Mid-infrared suspended membrane waveguide and ring resonator on silicon-on-insulator," *IEEE Photon. J.* **4**, 1510–1519 (2012).
20. Y. Xia, C. Qiu, X. Zhang, W. Gao, J. Shu, and Q. Xu, "Suspended Si Ring Resonator for Mid-IR Application," *Opt. Lett.* **38**(7), 1122–1124 (2013).
21. C. Reimer, M. Nedeljkovic, D. J. M. Stothard, M. O. S. Esnault, C. Reardon, L. O'Faolain, M. Dunn, G. Z. Mashanovich, and T. F. Krauss, "Mid-infrared photonic crystal waveguides in silicon," *Opt. Express* **20**(28), 29361–29368 (2012).
22. R. Shankar, R. Leijssen, I. Bulu, and M. Lončar, "Mid-infrared photonic crystal cavities in silicon," *Opt. Express* **19**(6), 5579–5586 (2011).
23. Y. Zou, S. Chakravarty, L. Zhu, and R. T. Chen, "The role of group index engineering in series-connected photonic crystal microcavities for high density sensor microarrays," *Appl. Phys. Lett.* **104**(14), 141103 (2014).
24. Y. Zou, S. Chakravarty, D. N. Kwong, W.-C. Lai, X. Xu, X. Lin, A. Hosseini, and R. T. Chen, "Cavity-waveguide coupling engineered high sensitivity silicon photonic crystal microcavity biosensors with high yield," *IEEE J. Sel. Top. Quantum Electron.* **20**(4), 1–10 (2014).
25. R. Shankar, I. Bulu, and M. Loncar, "Integrated high-quality factor silicon-on-sapphire ring resonators for the mid-infrared," *Appl. Phys. Lett.* **102**(5), 051108 (2013).
26. B. J. Frey, D. B. Leviton, and T. Madison, "Temperature-dependent refractive index of silicon and germanium," *Proc. SPIE* **6273**, 62732J (2006).
27. S. Rahimi, A. Hosseini, X. Xu, H. Subbaraman, and R. T. Chen, "Group-index independent coupling to band engineered SOI photonic crystal waveguide with large slow-down factor," *Opt. Express* **19**(22), 21832–21841 (2011).
28. M. von Edlinger, J. Scheuermann, L. Nähle, C. Zimmermann, L. Hildebrandt, M. Fischer, J. Koeth, R. Weih, S. Höfling, and M. Kamp, "DFB interband cascade lasers for tunable laser absorption spectroscopy from 3 to 6 μm ," in *SPIE OPTO (International Society for Optics and Photonics, 2013)*, pp. 899318–899319.
29. W. J. Marinelli, C. M. Gittins, A. H. Gelb, and B. D. Green, "Tunable Fabry-Perot etalon-based long-wavelength infrared imaging spectroradiometer," *Appl. Opt.* **38**(12), 2594–2604 (1999).
30. M. Ahmed and M. Yamada, "Design Method for Optical Waveguide Filters Having Corrugation Structures by Corrugation Width Modulation," *Opt. Rev.* **4**(3), 402–407 (1997).

1. Introduction

Silicon has been the material of choice of the photonics industry over the last decade due to its easy integration with silicon electronics as well as its optical transparency in the near-infrared telecom wavelengths. In recent years, photonic devices on chips are increasingly being used for chemical and biological sensing. Ring resonators [1], photonic crystal waveguides (PCWs) [2], photonic crystal (PC) microcavities [3] operating at 1.55 μm have been employed for biosensing. Optical biosensors can be theoretically designed for operation at any wavelength after taking into consideration the absorbance of water based biological media. In contrast, chemicals are best recognized by their unique wavelength specific optical absorption signatures. Slow light in PCWs [4] and PC slot waveguides [5, 6] has been used to reduce the optical absorption path length and achieve high detection sensitivity in on-chip optical absorption spectroscopy for the selective detection of volatile organic compounds [4, 5] and greenhouse gases [6] based on unique analyte absorption signatures in the near-infrared (near-IR). It is common knowledge that in contrast to the near-infrared, the mid-infrared (mid-IR) wavelengths offer at least two orders of magnitude larger absorption cross-sections than the near-IR. Silicon is optically transparent from 1.1 μm to 8 μm [7, 8]. Hence, PCWs and PC slot waveguides in silicon-on-insulator (SOI) (from 1.1 μm to 3.7 μm), silicon-on-sapphire (SoS) (from 1.1 μm to 5.5 μm) and free-standing silicon membranes (from 1.1 μm to 8 μm) can serve as the ideal platform for highly sensitive optical absorption spectroscopy on chip. Strip [9–15] and slot waveguides [16, 17] have been demonstrated by several groups in the mid-IR

in silicon on both SOI and SoS. Some devices have also been demonstrated in the mid-IR in free-standing silicon platform [18–20]. In spite of available material platforms and laser sources in the mid-IR, PC research in the mid-IR has been limited by the unavailability of appropriate tunable laser sources that can characterize the entire PC transmission bandwidth [21, 22]. Optical parametric oscillators (OPOs) are suitable sources for mid-IR optical devices. However OPOs are relatively expensive and bulky and cannot therefore be used for any realistic sensing system outside the lab [21].

In this paper, we present the first experimental demonstration of the propagation characteristics of a mid-IR photonic crystal waveguide (PCW) in SoS with a fixed wavelength 3.43 μm Fabry-Perot interband cascade laser (ICL). We demonstrate that by good control of device fabrication and device parameter engineering, PC waveguiding properties can be adequately determined in PC devices and thereby facilitate the accurate design of PC sensors in all wavelength bands from visible to far-infrared. Previously PC microcavities and PCWs have been demonstrated in free-standing silicon membranes in SOI in the mid-IR wavelengths [21, 22]. While free-standing membranes in SOI can guide light over a larger wavelength range, fabrication yield of such suspended membrane structures is low. Furthermore, photonic crystal waveguide lengths will be limited by the bending frequently observed in free-standing membranes. The SoS platform is therefore more robust for photonic sensing applications in the mid-IR compared to fragile, free-standing silicon membranes in SOI.

2. Design and fabrication

The device comprises a conventional W1 PCW with a single missing row of holes along the Γ –K direction in a hexagonal lattice of air holes in silicon. Figure 1(a) shows the simulated transmission spectrum of a W1 PCW with lattice constant $a = 845$ nm, radius of air holes $r = 0.25a$ and height of silicon slab $h = 0.69a$ obtained by three-dimensional (3D) finite difference time domain (FDTD) simulation. Refractive indices of silicon and sapphire were considered as 3.429 and 1.7 respectively. A distinct transmission band edge is observed at $\lambda = 3.445$ μm . A conventional experimental demonstration of the transmission spectrum would simply comprise sweeping the wavelength range with a tunable spectrum and detector, or spectral identification via a spectral analyzer and a broadband source. However, it is also possible to characterize the PCW transmission characteristics by careful control of design and fabrication, and sweeping the lattice constant a . Figure 1(b) shows a set of FDTD simulations of a short W1 PCW with length 50 μm and different lattice constant. The radius r was kept fixed at $0.25a$. The height of the silicon device layer according to wafer specifications is 600 ± 60 nm. In this work, the height of the silicon device layer was determined to be $h = 585 \pm 1$ nm from ellipsometry. h/a of the silicon slab was calculated accordingly for each lattice constant. The wavelength spectrum of our Fabry-Perot ICL is shown by the dashed black line.

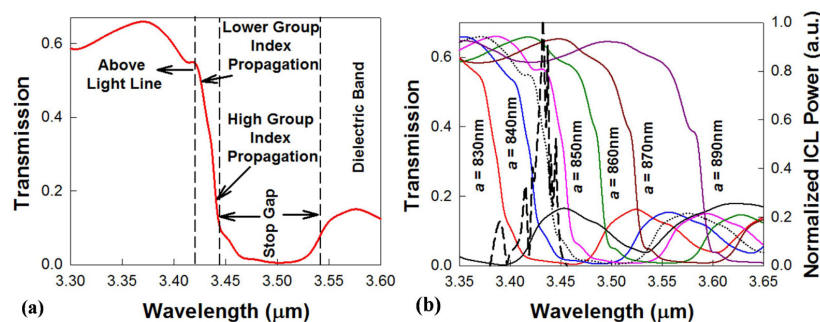


Fig. 1. (a) 3D FDTD simulation of a short W1 PCW in silicon-on-sapphire for operation at 3.43 μm with $a = 845$ nm. The different parts of the transmission spectrum are indicated. (b) Set of 3D FDTD simulations of short W1 PCWs with different lattice constants $a = 830$ nm, 840 nm, 845 nm, 850 nm, 860 nm, 870 nm and 890 nm. Simulation for $a = 845$ nm is indicated by the dotted black plot. The output spectrum of our source ICL is indicated by the dashed black plot (right axis).

Light is guided in and out of the PCW by strip waveguides with PC group index taper to enable high coupling efficiency into the slow light guided mode [23, 24]. Figure 2 shows the dispersion diagram of the W1 PCW obtained by 3D plane-wave expansion simulation. Figure 1(b) indicates that the ICL emission will propagate in the high group index regime in devices with $a = 845$ nm. Figure 2 is thus calculated with $a = 845$ nm. The dispersion diagram shows the guided mode (in red) separated from the dielectric band by a stop gap. The light line for sapphire is superimposed. The PC group index taper is created by gradually tapering down the width of the PCW from the interface between the strip waveguide and PCW over 8 lattice periods from W1.07 to W1. W1.07 indicates that the width of the PCW at the onset of the taper is $1.07 \times \sqrt{3}a$. The red dashed plot in Fig. 2 shows the dispersion of the guided mode when the PCW is W1.07. Two dashed blue lines are drawn on the dispersion plots of the guided mode at the representative frequency $a/\lambda = 0.246$. The slope of the lines $\delta k/\delta \omega$ gives the group indices (8 and 30 respectively) for W1.07 and W1 PCW, where k is the wave vector and ω is the frequency. Hence instead of coupling light from the strip waveguide to the W1 PCW at a group index $n_g = 30$ at $a/\lambda = 0.246$ in Fig. 2, group index taper engineering results in light coupled from the strip waveguide into the PCW at $n_g = 8$. It has been shown in the near-IR that such group index engineering reduces Fresnel reflection losses that would otherwise show significant fringe patterns in the PCW guided mode transmission spectrum [23].

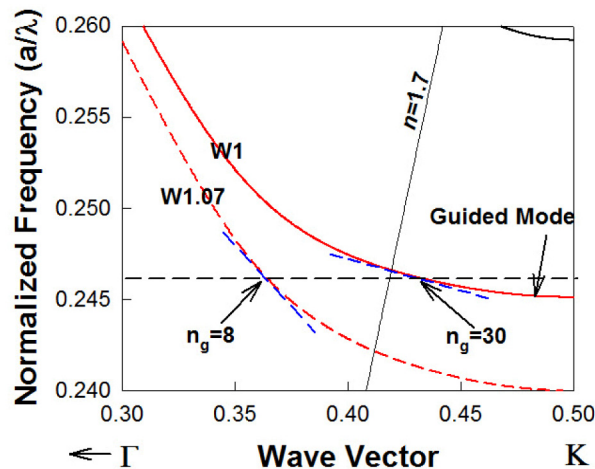


Fig. 2. 3D plane wave expansion simulation of the dispersion diagram of a silicon based W1 PCW on sapphire substrate with air top cladding. The red dashed line indicates the PCW dispersion at the interface between silicon strip waveguide and W1.07 PCW. The reduced group index at the interface is indicated by the lesser slope (dashed blue lines) at a representative frequency $a/\lambda = 0.246$. Sapphire light line is superimposed.

Devices were fabricated using a combination of electron beam lithography and inductively coupled plasma etching. Input and output strip waveguides and sub-wavelength grating (SWG) couplers are fabricated in the same step as the PCW. The design, fabrication and experimental characterization of strip waveguides and SWGs in SoS have been described in detail elsewhere [17]. In order to ensure good control over the fabrication process, a thin conductive polymer (ESPACER) from ShowDenko chemicals was spin coated on the ebeam resist ZEP-520A, prior to ebeam lithography. The chip is cleaned using Piranha for 15 minutes and followed with three cycles of Piranha/HF post-process treatment [25]. Microscope image of the complete device with input and output SWGs is shown in Fig. 3(a). In Figs. 3(b)–3(c), scanning electron micrograph (SEM) images show the device top view and tilted view showing the etched air holes. SEMs of the input and output group index tapers implemented by tapering the width of the PCW from W1.07 at the strip waveguide-PCW interface to W1 in Fig. 3(e) are shown in Figs. 3(d) and 3(f) respectively.

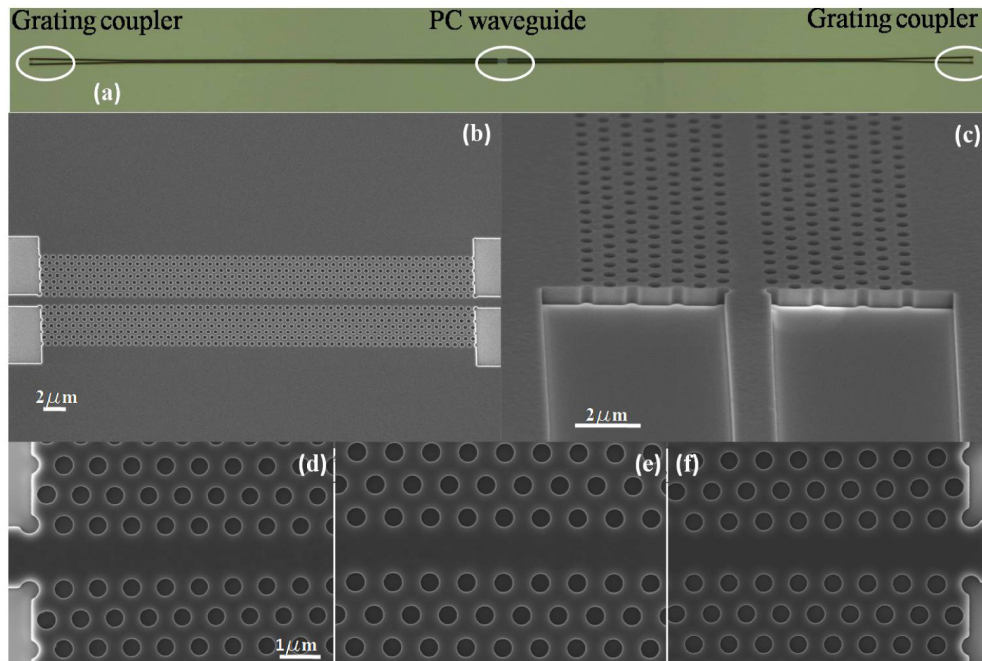


Fig. 3. (a) Microscope image of the device showing input and output SWGs and PCW. (b) Top view SEM image of PCW and (c) side view SEM image of the PCW at the PCW-strip waveguide interface. Magnified top view SEM images of (d) input group index taper (e) PCW and (f) output group index taper.

3. Results and discussion

Devices are characterized using the experimental setup described in [17]. As shown in Fig. 4, light emitted from a continuous-wave ICL from Thorlabs, with a fixed wavelength of 3.43 μm , is passed through a pair of ZnSe lenses and coupled into a 9/125 μm single mode ZrF₄ optical fiber from Thorlabs. Light from the optical fiber is then coupled into the fabricated chip via SWG couplers. At the output end, another SWG coupler couples the light from chip to the output fiber. An InSb detector is used to measure the power from the output fiber. To improve coupling efficiency, we put a focus lens between the end of output fiber and InSb detector. In order to improve the signal-to-noise ratio, a mechanical chopper is used with chopping frequency of 1 KHz, and the detected signals from InSb are demodulated by a lock-in amplifier.

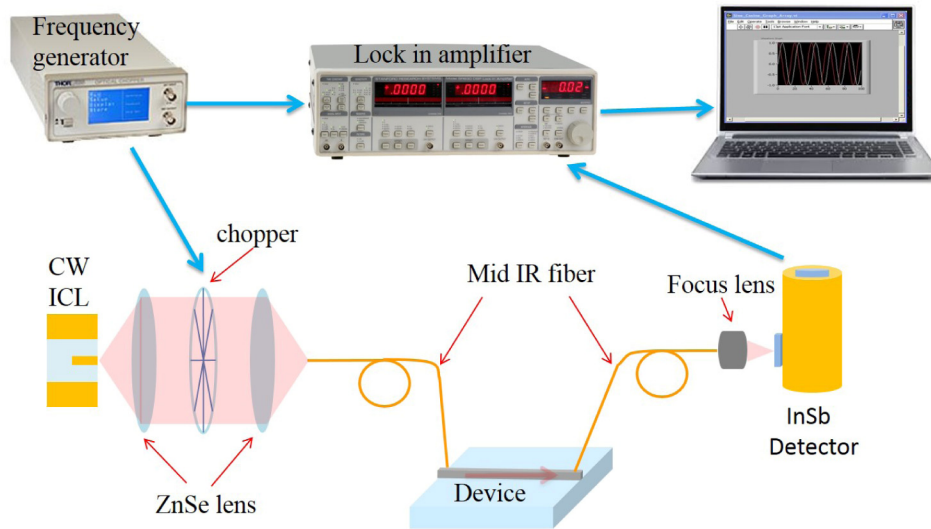


Fig. 4. Schematic of the experimental setup used to characterize our device

The light from the output SWG for PCW devices with several lattice constants but the same r/a is plotted in Fig. 5(a) with air as top cladding. The length of the W1 PCW is 50 μm . The plot is normalized with respect to the highest and lowest power observed versus lattice constant. It is observed that for a less than 845 nm, the output power from the devices is practically zero. Figure 5(a) also plots the output power from the devices when immersed in tetrachloroethylene (C_2Cl_4). C_2Cl_4 is practically non-absorbing at 3.43 μm with a refractive index ~ 1.5 at room temperature. The absolute power measured by the photodetector is lower with C_2Cl_4 than with air cladding in Fig. 5(a) due to the lower modal confinement; however the normalized plot shows the transmission profile shifted to lower lattice constants. Figure 5(b) plots the output power as a function of temperature for varying lattice constant. The temperature is varied from 25 $^\circ\text{C}$ to 60 $^\circ\text{C}$. The normalized plot also shows a shift of the transmission profile to lower lattice constants, with increasing temperature.

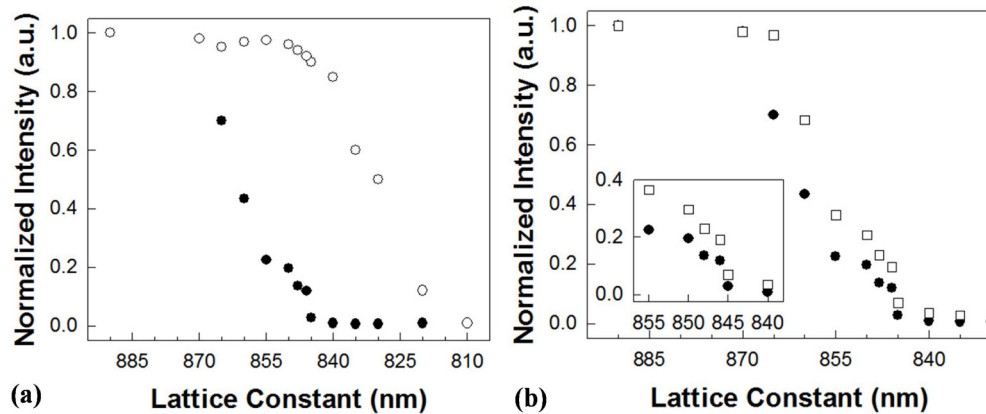


Fig. 5. (a) Normalized transmitted intensity through an air-clad W1 PCW in SoS with $r = 0.25a$, as a function of a at $\lambda = 3.43 \mu\text{m}$ plotted (a) in air (bold circles) and C_2Cl_4 (open circles) and (b) as a function of temperature at 25 $^\circ\text{C}$ (bold circles) and 60 $^\circ\text{C}$ (open squares). Inset in (b) magnifies the data for devices between $a = 840 \text{ nm}$ and $a = 855 \text{ nm}$.

At $a = 840 \text{ nm}$ and lower, the probed wavelength of 3.43 μm is clearly within the photonic band gap; hence the transmitted power is zero. At lattice constants from $a = 845 \text{ nm}$ to $a =$

850 nm, the fixed wavelength ICL probes the W1 PCW guided mode at gradually decreasing group indices which translates experimentally to gradually increasing transmitted power. At a greater than 850 nm, the probed wavelength propagates above the light line and the transmitted power reaches a maximum for the short W1 PCWs.

When the cladding refractive index is increased from $n = 1$ in air to $n = 1.5$ in C_2Cl_4 , the W1 PCW guided mode is shifted down towards the dielectric band in Fig. 2. All simulated curves in Fig. 1(b) are shifted to longer wavelengths. As a result, the 3.43 μm fixed wavelength source can be propagated through PCWs with smaller lattice constants. The phenomenon is experimentally observed by the shift of the transmitted intensity vs. lattice constant curves to shorter lattice constants. The experimental results were validated via simulation results in Figs. 6(a) and 6(b) wherein a large increase in transmission was observed for representative lattice constants $a = 845$ nm and $a = 830$ nm. For $a = 810$ nm, the simulated transmission intensity in Fig. 6(c) shows some transmission via the dielectric band at the wavelength of the source laser at 3.43 μm . However, experimentally, the slab guided mode is too weak in intensity; hence nearly zero transmission is experimentally observed in both air and C_2Cl_4 . The simulated results match with experimentally observed increase in transmission intensities characteristic of shift of the W1 guided mode transmission band edge to smaller lattice constants.

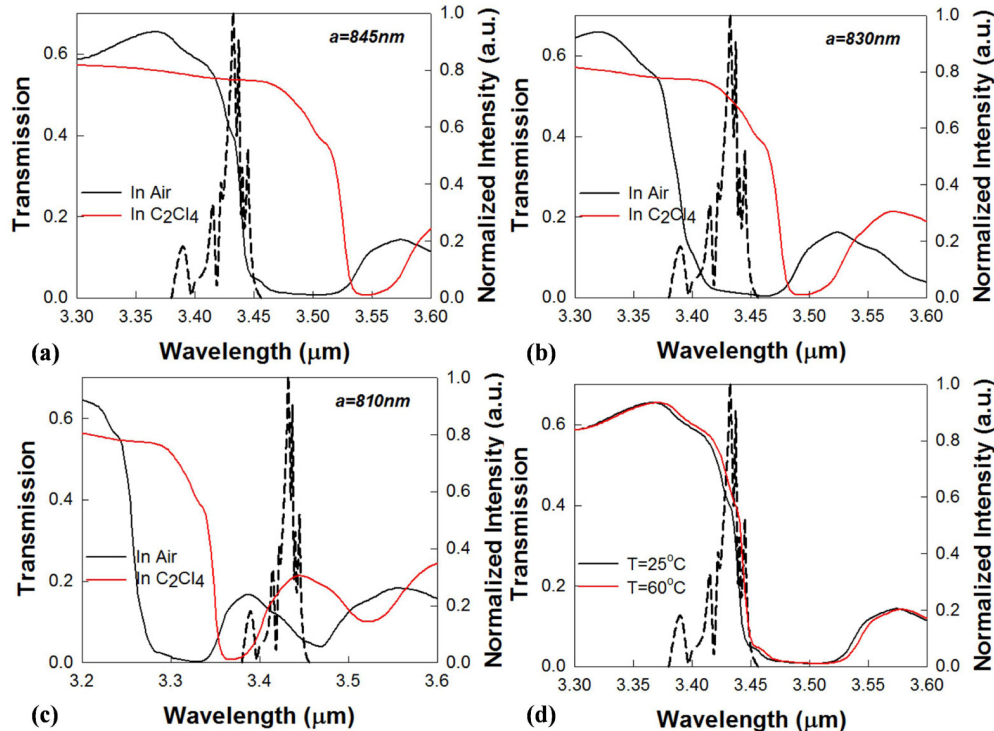


Fig. 6. 3D FDTD simulated transmission spectra through a 50 μm long PCW in SoS in air (black) and C_2Cl_4 (red) for (a) $a = 845$ nm, (b) $a = 830$ nm, (c) $a = 810$ nm and (d) for a change in temperature from 25 $^\circ C$ (black) to 60 $^\circ C$ (red) for $a = 845$ nm. The transmission of the source laser is shown for comparison.

The effect of temperature can be similarly explained. Silicon has a positive temperature coefficient of refractive index at 3.43 μm [26]. An increase in temperature increases the silicon refractive index so that the W1 PCW guided mode is again shifted down in frequency in the normalized dispersion diagram in Fig. 2. As a result, the 3.43 μm source can be transmitted through PCWs with smaller lattice constants as temperature is increased, as observed in Fig. 5(b). The shifts in the plots in Fig. 5(b) due to change in temperature from 25

°C to 60 °C are much smaller than the shift in the plots in Fig. 5(a) due to change in refractive index by C₂Cl₄ and is validated via the simulated transmission profiles versus temperature of our short W1 PCW in Fig. 6(d).

An exact one-to-one mapping of the simulated and experimentally observed transmitted intensities in Figs. 5 and 6 is complicated by the fact that the 3D FDTD simulation does not take into account the minimum detectable signal by the photodetector. From Fig. 1(b), we note that the simulated transmitted intensity in air for $a = 845$ nm at the ICL wavelength is 65% of the maximum transmitted intensity. However, experimental results in Fig. 5(a) indicate that the transmitted intensity for $a = 845$ nm is only 2.8% of the maximum experimentally observed transmitted intensity for devices with $a > 860$ nm. The difference arises from the propagation loss at high group indices, which limits the signal measured by the photodetector. However, simulations in Fig. 6 together with experimental results in Fig. 5 clearly validate the observed increase in transmitted intensities in C₂Cl₄ versus corresponding transmitted intensities in air due to the shift in the transmission band edge to longer wavelengths with increased refractive index. To accurately determine the bandwidth of the photonic crystal waveguide guided mode, it is therefore necessary to determine the position of the light line.

The position of the light line was validated by propagation loss measurements in Fig. 7. Devices with lengths varying from 50 μm to 400 μm were fabricated with different lattice constants as shown in Table 1. It was ensured from ellipsometry that the selected chips for fabrication had silicon height $h = 585 \pm 1$ nm. Figure 7(a) plots the corresponding propagation losses versus lattice constant. The measured propagation losses were summarized in Table 1. At a greater than 855 nm, the propagation loss increases rapidly with increasing length of the PCW, reaching as high as 680 dB/cm for $a = 870$ nm. It can thus be concluded that the ICL emission propagates above the light line for devices with a greater than 850 nm. The waveguide mode above the sapphire light line in the 2D PCW region propagates along the line defect due to the existence of the in-plane photonic bandgap. At the same time, the waveguide mode above the light line couples to the continuum of radiation modes and is thus continually radiated out of plane into the substrate. However, the devices in Fig. 5 are only 50 μm (~ 60 periods) long and n_g is small above the light line as observed from Fig. 2. Hence, for short PCWs, higher transmission is observed above the light line than below the light line where the PC waveguide mode is confined both laterally and vertically. As the PCW become longer, the out-of-plane losses dominate leading to huge propagation loss above the light line.

In Fig. 7(b), we estimate the approximate propagation group index at the ICL wavelength of 3.43 μm for different lattice constants, by plotting the group index profile of the W1 PCW guided mode versus wavelength from Fig. 2. The guided mode dispersion profile in Fig. 2 and thus the n_g profile versus wavelength is changed minimally with different h/a for the range of lattice constants studied here. The guided mode is shifted down in frequency with increasing a while h is nearly constant at 585 nm. The n_g plot is shifted versus a by the same wavelength magnitude as the offset of the transmission band edge in FDTD simulations in Fig. 1(b). We observe from Fig. 2 that at the intersection of the light line with the PCW guided mode, $n_g \sim 23$. We thus estimate that in the $a = 850$ nm device, light propagates with $n_g \sim 23$. Since the n_g plot would just be shifted versus wavelength for other lattice constants, from the offsets calculated from Fig. 1(b), we estimate from Fig. 6(b) that at $a = 846$ nm and $a = 848$ nm, light propagates with n_g approximately 30 and 27 respectively. The above propagation losses are better than 20 dB/cm measured in [21] at $n_g = 5$. A W1 PCW with $a = 845$ nm, $r/a = 0.25$ and $h/a = 0.69$ in SoS would be expected to show similar propagation characteristics with a tunable laser source covering the wavelength range in Fig. 6(b).

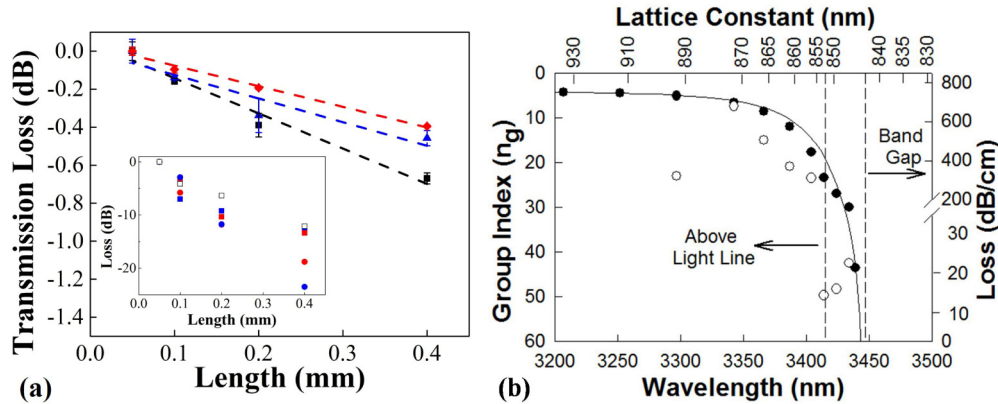


Fig. 7. (a) Transmission losses in W1 PCWs in SoS below the light line for $a = 846$ nm (■), $a = 848$ nm (▲) and $a = 850$ nm (◆) at $\lambda = 3.43$ μm . The three dash lines are the linear fit for $a = 846$ nm (black), $a = 848$ nm (blue), and $a = 850$ nm (red). Inset plot the propagation losses above the light line for devices with $a = 855$ nm (■), 860 nm (■), 865 nm (●), 870 nm (●) and 890 nm (□). (b) Solid line plot is the group index profile versus wavelength for W1 PCW in Fig. 2 with $a = 845$ nm. Estimated propagation group indices versus lattice constant are plotted with filled circles. Experimental propagation losses for measured devices are plotted versus lattice constant with open circles (right axis).

Table 1. Summary of measured lattice constants and its corresponding propagation loss

Lattice Constant (nm)	846	848	850	855	860	865	870	890
Propagation Loss (dB/cm)	18	15	12	320	370	510	680	320

The success of the present method for PCW device characterization using a single wavelength laser source does rely on the accurate control of device parameters in design and fabrication. The mean square error in determining the height of the silicon device layer in ellipsometry is less than 6\AA . The results presented here were achieved over 3 chips for each of which the silicon layer thickness is 585 ± 1 nm. While the lattice constant is controlled accurately by design and default lithography stage motion to a few angstroms, the use of ESPACER in fabrication on the SoS substrates ensures that the measured diameter of the fabricated PC air holes is accurate to with ± 2.5 nm conservatively. 3D FDTD simulations in Fig. 8 indicate that for propagation above the light line, the variation in the simulated transmitted intensity due to a 5 nm variation in air hole diameter is less than 5% for a greater than 855 nm. Below the light line, a variation of 5 nm in diameter at $a = 845$ nm results in a 7 nm shift in the simulated transmission band edge. The value is smaller than 18 nm simulated shift in the transmission band edge due to a change of 5 nm in the lattice constant around $a = 845$ nm, as observed from Fig. 1(b). An exact comparison versus experimental data, below the light line, is complicated due to the broad nature of the lasing spectrum from the source laser as shown in the figures. Considering the peak wavelength of the source laser, it is estimated from 3D FDTD that the error in transmission intensity due to diameter variation by 5 nm below the light line should be less than 12%.

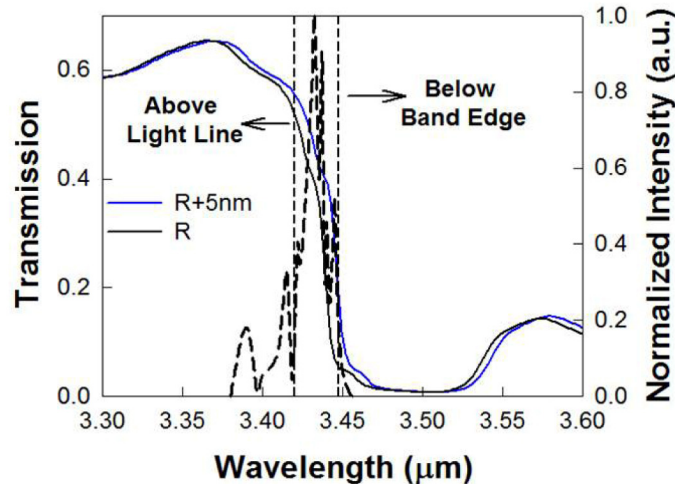


Fig. 8. 3D FDTD simulated transmission spectra through a 50 μm long PCW in SoS at $a = 845$ nm for radius $r = 0.25a$ (black) and radius $r = 0.25a + 5$ nm (blue). Short dashed lines indicate the positions of the light line and transmission band edge. The source laser spectrum is shown in black long dashed line.

One of the challenges of the SoS platform is the relatively high cladding index of sapphire which limits the PCW guiding bandwidth to only about 22 nm in the present design, as validated experimentally by the measurement of propagation loss and comparing with simulated transmission spectra. By lattice engineering the air hole diameter and PCW width, it is possible to obtain a larger PCW guiding bandwidth and is the object of future studies. Mid-infrared tunable laser sources with wavelength tuning step less than 2 nm, eases the fabrication tolerances and may enable PCW devices to be operated very close to the transmission band edge where $n_g \sim 35$ similar to near-infrared demonstrations [23]. However, in PCW devices for optical sensing applications in the mid-infrared, it is possible to design with a flat group index profile with $n_g = 25$, across a wide wavelength range as has been demonstrated across 22 nm wavelength range in the near-infrared [27]. The performance compromised by the difference in group index is not significant when also taking into account the higher propagation loss nearer to the transmission band edge.

The device characterization method demonstrated here can be further improved by the use of distributed feedback (DFB) ICLs [28] or tunable mid-infrared Fabry-Perot etalons [29]. DFB ICLs and Fabry-Perot etalons would narrow the linewidth from the present 10 nm linewidth at the 3 dB point of our commercially available Fabry-Perot ICL at 3.4 μm and would also remove the low intensity sidebands. Instead of expensive Fabry-Perot etalons, future work can consider the integration of waveguide bandpass filters [30] together with other integrated photonic structures to filter out unwanted sidebands. In the present work, as observed in simulations in Fig. 1(b), a lattice constant step of 5 nm causes more than 15 nm shift in the transmission band edge of the PCW. Since the PCW investigated here has a 22 nm bandwidth, the identification of guided mode transmission regions via propagation loss measurements was not affected for the coarse step of lattice constants selected. Elimination of the sidebands with monolithically or heterogeneously integrated DFB ICLs and chip-integrated bandpass filters would not only improve the propagation loss values calculated for the PCW guided mode, but would also make such a chip portable for field based mid-infrared sensing applications. The method demonstrated here can be used across any wavelength band from the visible to the far-infrared in appropriately chosen waveguide core materials.

4. Conclusion

We experimentally demonstrated the first PCW in SoS in the mid-IR, to the best of our knowledge, together with a new measurement method to overcome the limitations of tunable laser sources in the mid-IR for PCW characterization. By engineering the lattice constant, we experimentally demonstrated the transmission characteristics with a single wavelength source. In the guided mode region below the light line, propagation losses below 20 dB/cm were observed for group indices n_g greater than 20. We experimentally observed more than 300 dB/cm propagation losses above the light line and zero transmission in the stop band. Our experimental method enables the design of guided wave photonic structures, using miniature PC devices in the mid-IR, even in the absence of mid-IR tunable sources. The method can be extended to other wavelength ranges from the visible to the far-infrared.

Acknowledgments

The authors thank NSF for supporting this work (SBIR Grant #IIP-1127251). S.C., P.W. and R. C. also acknowledge Army SBIR Contract #W911SR-12-C-0046 for partially supporting this work.